

Solar cell heterojunctions for candidate absorbers enargite and bournonite from electronic band and lattice matching

Suzanne K. Wallace^{a,b}, Keith T. Butler^c, Yoyo Hinuma^{d,e}, and Aron Walsh^{*b,f}

^a Department of Chemistry, Centre for Sustainable Chemical Technologies, University of Bath, Claverton Down, Bath, BA2 7AY, UK

^b Department of Materials, Imperial College London, Exhibition Road, London SW7 2AZ, UK. Email: a.walsh@imperial.ac.uk

^c ISIS Neutron and Muon Source, Rutherford Appleton Laboratories, Didcot, Oxfordshire, OX11 0QX

^d Center for Frontier Science, Chiba University, Chiba 263-8522, Japan

^e Center for Materials Research by Information Integration, Research and Services Division of Materials Data and Integrated System, National Institute for Materials Science, Tsukuba 305-0047, Japan

^f Department of Materials Science and Engineering, Yonsei University, Seoul 03722, Korea

Received Xth XXXXXXXXXX 20XX, Accepted Xth XXXXXXXXXX 20XX

First published on the web Xth XXXXXXXXXX 200X

DOI: 10.1039/b000000x

A vital part of the development of efficient solar cell devices to take candidate photovoltaic (PV) absorber materials from the lab benchtop through to commercial solar cell devices is the optimisation of the full device architecture, layer-by-layer. We recently proposed the naturally occurring minerals enargite (Cu_3AsS_4) and bournonite (CuPbSbS_3) as materials that are stable with desirable optoelectronic properties for use as the absorber layer in a thin-film PV device. Additionally, the internal electric fields and possible ferroelectricity of these materials may allow for enhanced carrier separation and novel PV effects. In this work, we aim to accelerate the optimisation of solar cell devices made from these materials. We calculate the ionisation potential of the materials and propose suitable junction partners for forming a solar cell heterojunction with each absorber by matching the electronic band edges to a set of candidate contact materials. We then screen these candidates further by matching the lattices of the two materials to limit ourselves to only those that are likely to minimise strain and achieve good epitaxy. This two-step screening procedure reduced a dataset of 173 semiconductor materials to ~ 5 candidate junction partners for each surface termination of enargite and bournonite.

1 Introduction

Solar power is a very attractive contender as a source of sustainable electrical power. Technological breakthroughs to enable high-efficiency photovoltaic (PV) devices without the need to use scarce material components and with low manufacturing costs could secure solar power as a viable future power source. Exploiting ferroelectricity in photoactive ('photoferroic') materials could provide new pathways to high-efficiency PV devices. Phenomena referred to as 'anomalous' and 'bulk' PV effects in polar materials have demonstrated photovoltages orders of magnitude greater than the optical band gap and photocurrents in bulk, single-crystal absorbers in the absence of a typical p-n junction for carrier separation^{1–3}. On-going research efforts are exploring the theory behind these observed phenomena in photoferroic materials^{4–6}. However, even in polar crystals that do not exhibit ferroelectricity, the internal electric fields could enhance carrier separation and suppress electron-hole recombination⁷.

We recently identified three naturally-occurring minerals

as candidate photoferroic materials based on their optical band gaps and polar crystal structures⁸, including enargite (Cu_3AsS_4) and bournonite (CuPbSbS_3). To our knowledge, to date only one study has made solar cells out of any of these materials. In Ref. 9 solar cells were made from solution processed enargite using a device architecture developed for $\text{Cu}(\text{In,Ga})\text{Se}_2$ (CIGS) solar cell technology. In this study the authors list non-optimal band alignment of the absorber layer with the device architecture as a likely limitation of the current solar cell performance. This has been shown to be the case for CuSbS_2 solar cells also using device architecture optimised for CIGS absorber layers¹⁰. More mature technologies, such as CIGS-based devices, are still being continually optimised through improved band alignment with the n-type buffer layer¹¹ and non-optimal band alignment is also being considered as a possible limiting factor on the performance of $\text{Cu}_2\text{ZnSn}(\text{S,Se})_4$ -based solar cells¹². The development of an optimal device architecture for a new solar cell technology is a challenging and time-consuming process.

For many of the materials being studied for use as absorber

layers in thin-film solar cells, such as chalcogenide-based materials, it is not possible, or is very difficult, to achieve ambipolar doping. Therefore to achieve a p-n junction for many thin-film PV devices it is necessary to form an interface between two different materials with different optical band gaps, lattice constants and even slightly different crystal structures¹³. In the extreme case when the two materials are poorly matched, differences in lattice constant and crystal structure at a heterojunction interface can introduce a large strain, resulting in poor epitaxy at the interface¹⁴. Even for less extreme differences, small lattice mismatch at an interface generally introduces intra band gap defect states, which enhances Shockley-Read-Hall recombination, increasing dark currents and reducing the open circuit voltage of the device¹⁵.

In this work, we aim to accelerate the optimisation of solar cell device architectures for enargite (Cu_3AsS_4) and bournonite (CuPbSbS_3) by screening for candidate junction partners that could have optimal electronic band offsets and crystal lattices well-matched to minimise strain at the interface. The principles behind our screening criteria for optimal band offsets are outlined in the next section. Where there is no literature consensus as to whether the material is likely to be more easily doped p-type or n-type we screen for candidate contacts based on the relevant band offset for forming a solar cell junction for both cases.

2 Band offsets for solar cell heterojunctions

The band alignment at a solar cell junction is crucial to facilitate the separation of photo-excited electrons and holes to allow for extraction of the charge carriers before recombination can occur¹⁸. Although the internal electric fields in the materials in this study may allow for the bulk photovoltaic effect (where the electrical asymmetry at a junction is not required for a photocurrent to be generated), a heterojunction would provide a global driving force for carrier separation towards collection electrodes, while internal electric fields from the polar crystal structure could enhance carrier separation locally.

Junctions are classified as type I, II or III based on their band alignments, however only type I and type II are of interest for PV applications. A type II ‘staggered’ junction can also be referred to as a ‘cliff-like’ offset and a type I ‘straddling’ junction can also be referred to as a ‘spike-like’ offset, as illustrated schematically in Fig 1. For a p-type absorber layer, the minority carriers are electrons promoted into the conduction band (CB) of the absorber, therefore the transport of electrons from the CB of the p-type absorber to the junction partner is important for determining device performance. The parameter of interest here is the conduction band offset (CBO) between the two materials. However, for n-type absorbers it is photo-excited holes that are the minority carriers and so the magnitude

of the valance band offset (VBO) between the n-type absorber and the junction partner that is important for charge extraction.

It has been observed that for the p-type absorbers CIGS and CdTe, solar cell p-n junctions with a type I ‘spike’ offset (with a CBO producing a small barrier within the range of 0.1 and 0.3 eV), as shown in Fig. 1a, is a more defect-tolerant interface and gives better device performance^{16,21}. The central idea to this ‘defect-tolerant interface’ is that a small positive spike CBO creates an absorber inversion layer, resulting in a large hole barrier at the interface¹⁶, whilst only creating a modest barrier to electron transport across the interface so that electrons may still tunnel across the interface¹⁵. Electron-hole recombination at an interface with high defect densities is then thought to be suppressed due to an insufficient hole supply at the interface. In contrast, for a type II or ‘cliff’ offset where the CBO is negative, as shown in Fig 1b, there may be high concentrations of holes in the vicinity of the interface to assist interface recombination, thereby reducing the open circuit voltage¹⁶.

For the n-type absorber ZnSnN_2 the opposite trend has been observed, where a spike VBO is expected to give a poorer performance¹⁷. In the case of ZnSnN_2 , it is believed that a spike offset may provide too large of a barrier to minority charge carrier transport across the interface due to the larger effective mass of minority-carrier holes (compared to typical effective masses for minority-carrier electrons in CIGS and CdTe²²) and associated lower hole mobility¹⁷. For ZnSnN_2 , a ‘small cliff’ is thought to be the optimal band alignment to avoid the barrier to charge transport from a spike offset but without the open circuit voltage (V_{OC}) being limited too greatly as would be the case for a ‘large cliff’. This can be seen from the decrease in qV_{OC} relative to the absorber band gap (E_g) in the cliff offsets in Fig. 1. Therefore in this study, we use calculated effective masses to inform our choice of optimal band offsets for forming solar cell heterojunctions.

3 Methodology

3.1 Electronic band and lattice matching

Screening for candidate heterojunction partners based on electronic band offsets and minimum lattice strain is conducted using the methodology and dataset of tabulated ionisation potentials (IPs) and electron affinities (EAs) for candidate junction partners in Ref. 14. This dataset contains the electronic band gaps, IPs and EAs of 173 candidate heterojunction partners obtained either from experimental measurements or electronic structure calculations. The rationale for our electronic screening step to find candidate junction partners for absorber layers is outlined next. For p-type (n-type) absorbers we screen for candidates junctions partners based on the CBO (VBO). We

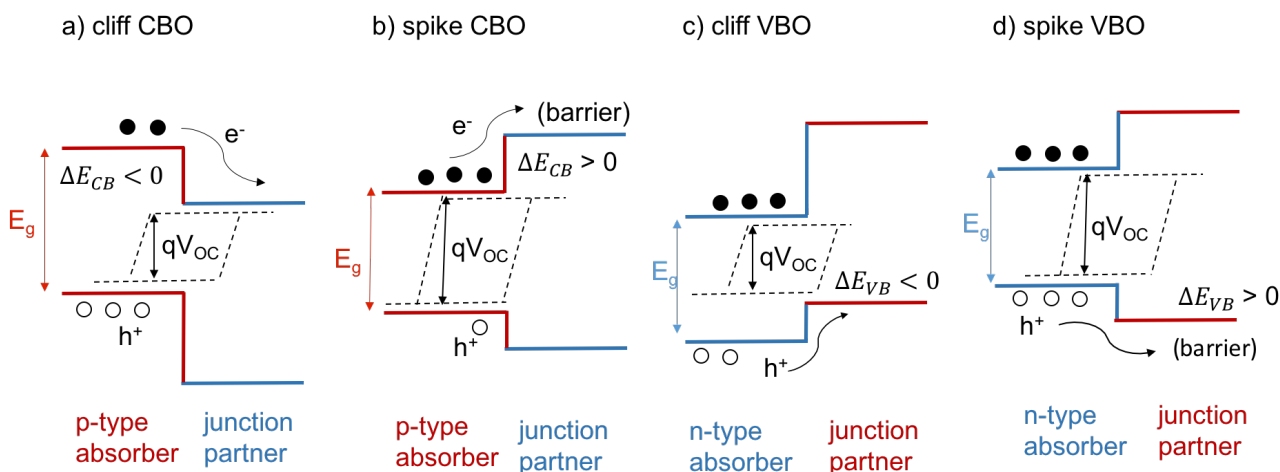


Fig. 1 Illustration of four possible junctions present in a solar cell. a) A type II heterojunction between a p-type absorber and an n-type contact material where photoelectrons flow across the interface with no barrier at the negative ‘cliff’ conduction band offset (CBO), but the open circuit voltage is reduced relative to the absorber band gap if the cliff is large. b) A type I heterojunction between a p-type absorber layer and an n-type contact material with a small positive (‘spike’) CBO. If the spike is small enough electrons can tunnel through the barrier and across the interface. Holes are repelled from the interface region. c) A type II heterojunction between an n-type absorber and a p-type contact material where photoelectrons flow across the interface with no barrier at the negative ‘cliff’ valence band offset (VBO), but the open circuit voltage is reduced relative to the absorber band gap if the cliff is large. d) A type I heterojunction between an n-type absorber layer and a p-type contact material with a small positive (‘spike’) VBO. If the spike is too large this barrier will impede transport across the interface if hole mobility is low. Figures adapted from Ref. 16 and 17.

look for a small cliff offset in all cases by looking for a band offset in the range 0 to -0.3 eV. However for cases where the minority carrier effective mass calculated in Ref. 8 is less than $0.5m_e$ we also look for a small spike offset in the range +0.1 to +0.3 eV. A small barrier to minority carriers crossing junction is negligible if carriers are able to tunnel through it¹⁵. For CIGS +0.2 eV has been reported to be optimal²¹ and +0.3 eV for CdTe¹⁶.

We limit our search to candidate junction partners where an interface with strain less than 4% is obtained. We consider no defect states at the interface and allow no intermixing at the interface, which is known to be present to a large extent at the CdTe:CdS interface²³ and has been shown to affect the defect physics of the interface²⁴. However, for final candidate contacts we speculate the likely extent of interface intermixing based on the chemical similarities of the components of the two materials forming the heterojunction.

3.2 Band alignment

The alignment of the valence band energy to the vacuum level, i.e. the ionisation potentials (IPs), are physically well-defined quantities. IPs can be measured using techniques such as photoelectron spectroscopy or Kelvin probe microscopy and can be computed using first-principles calculations of surface slab models²⁵. The electron affinity (χ) is defined as the con-

duction band energy with respect to the vacuum level. This value can be obtained by adding the value of the electronic band gap onto the IP of the material. Experimental results from two decades of photoelectron spectroscopy experiments on CdTe and CIGS thin-film solar cells have been compared to density functional theory (DFT) calculations¹³, where it was found that the energy band alignments for many interfaces were in good agreement between the experimental and theoretical methods. However, for cases where there was poor agreement and in particular where deviations in measured and calculated band alignments were sensitive to interface preparation methods, this is thought to be related to the presence of high defect-concentrations in the materials forming the contact. For this reason, theoretically predicted band alignments are usually considered as the ‘intrinsic’ or ‘natural’ alignment for a particular combination of materials forming an interface¹³, i.e. that which could be expected to form naturally for a perfect interface, in the absence of defects. A predicted ideal band alignment therefore acts as a starting point to limit the search space for combinations of materials that are more likely to be suitable junction partners.

The model used to predict the energy band alignment at solar cell heterojunctions in this study is the electron affinity rule (also known as Anderson’s rule) where energies are aligned through an absolute vacuum level^{26,27}. This method does not account for possible interface effects, such as inter-

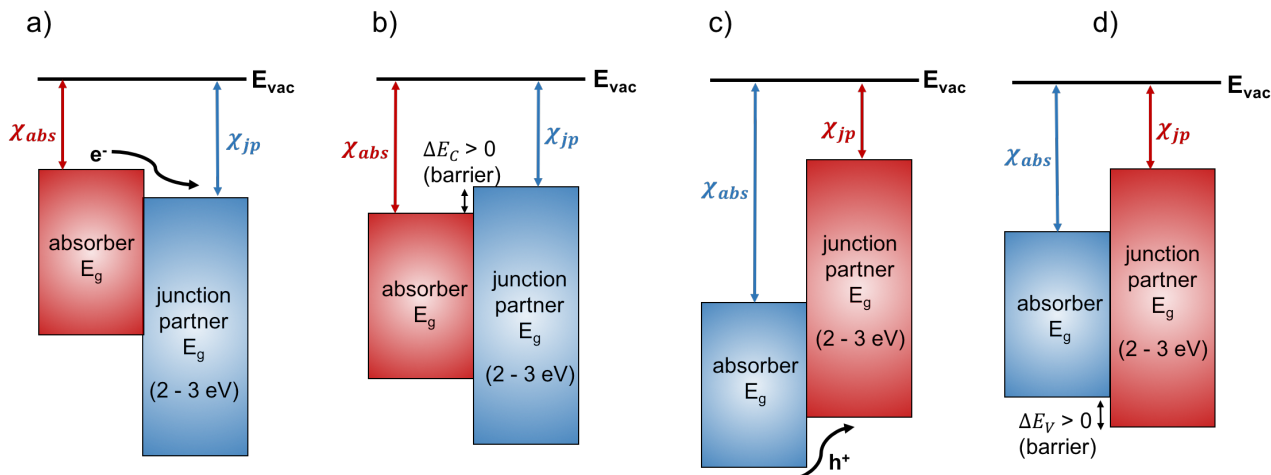


Fig. 2 Heterojunction alignments for solar cells with respect to the vacuum level, E_{vac} , based on the electron affinity (conduction band energy), χ_{abs} . a) Type II ‘staggered’ with a p-type absorber and no barrier to minority photocarrier transport across the junction, b) Type I ‘straddling’ with a p-type absorber and a small barrier (positive ΔE_c) to minority carrier transport, c) Type II ‘staggered’ with an n-type absorber and no barrier to minority photocarrier transport, d) Type I ‘straddling’ with an n-type absorber and a small barrier (positive ΔE_v) to minority carrier transport. Fig. adapted from Ref. 19 and 20.

mixing of species at a heterojunction, or consider the effects of finite temperature on band offsets²⁸. However, we discuss the likely impact of such effects for the most promising junction partner candidates later. To obtain the band offsets from the electron affinity rule, the vacuum level of the two heterojunctions either side of the heterojunction are aligned to the same energy, the difference between the distance between the CBM and the vacuum (χ) of each material is used to predict the CBO, as shown in Eq. 1. In this study we take semiconductor 1 to be the absorber with a band gap ($E_{g,abs}$) within the visible range (approximately 1.1 to 1.7 eV) and semiconductor 2 to be the transparent junction partner with a wider $E_{g,jp}$ in the range of 2-3 eV. If CBM_{jp} is closer to the vacuum level than CBM_{abs} then ΔE_c is positive, corresponding to a ‘spike’ CBO. If E_g of each material is also taken into account then the same model can be used to predict the VBO through the difference in the ionisation potentials ($IP = \chi + E_g$). If $E_{g,jp}$ is sufficiently larger than $E_{g,abs}$ such that VBM_{abs} is closer to the vacuum level than VBM_{jp} , then the VBO given by Eq. 2 is positive, corresponding to a ‘spike’ VBO. A heterojunction with both spike CBO and spike VBO corresponds to a ‘straddling gap’. A negative ΔE_c or ΔE_v corresponds to a cliff CBO or cliff VBO respectively, this is then a ‘staggered gap’. These different cases are illustrated schematically in Fig. 2.

$$\Delta E_c = \chi_{jp} - \chi_{abs} \quad (1)$$

$$\begin{aligned} \Delta E_v &= E_{g,jp} - E_{g,abs} - \Delta E_c \\ &= (\chi_{abs} + E_{g,abs}) - (\chi_{jp} + E_{g,jp}) \\ &= IP_{abs} - IP_{jp} \end{aligned} \quad (2)$$

3.3 Computational details

3.3.1 Slab models We compute the IPs and EAs of the absorbers in this study but use the tabulated values of these properties for candidate contact layers, mentioned in section 3.1. IPs are dependent upon the surface orientations, therefore we construct slab models for all possible symmetric, non-polar surface terminations of the materials using methodology in Ref. 29. We consider only non-polar surface models as these are the most energetically likely to form. Relaxation of the ion positions and volume of the unit cells are performed in VASP^{30,31} using the PBEsol functional³², projector augmented wave core potentials³³, without including spin-orbit coupling (SOC) and with symmetry fixed until forces on the atoms are converged to within 0.005 eV per Å. A plane wave cutoff energy of 350 eV is used and k -grid densities of $6 \times 6 \times 6$ and $4 \times 4 \times 4$ were used to sample the electronic Brillouin zone for a 16 atom unit cell of enargite (Cu_3AsS_4) and a 24 atom unit cell of bournonite (CuPbSbS_3) respectively. Slab models are then cut from the relaxed unit cells. Convergence tests for calculation settings and visualisations of the slab structures are given in the SI.

To inform our later discussion for which candidate junction partners are likely to be the most important for devices, we calculate the surface energies for the slab models using Eq. 3 where E_{bulk} is the total energy of the bulk crystal per formula unit, n is the number of formula units in the surface slab and A is the area of surface, of which there are two per slab model.

$$\gamma = \frac{E_{surf} - nE_{bulk}}{2A} \quad (3)$$

3.3.2 Ionisation potential and electron affinity calculations Calculations for planar averaged electrostatic potential of the slab models are also performed in VASP but using the HSE06 functional³⁴ with SOC and a single k -point is used to sample the slab along the finite dimension. To calculate the ionisation potentials, IP, of the surface slab models the macroscopic average technique from Ref. 25 is used.

The difference between the macroscopic average of the vacuum potential and the bulk-like region of the surface slab is used to obtain the surface dipole, D_s . The eigenvalue of the valence band maximum (VBM) of the bulk, ϵ_{VBM} and D_s are then used to obtain IP as shown in Eq. 4.

$$IP = D_s - \epsilon_{VBM} \quad (4)$$

Electron affinities, χ , in this study are then calculated by subtracting the electronic band gap calculated with the HSE06 functional from the IP calculated as outlined above. When computing the electrostatic potential of the slab models ion positions are fixed. The differences between the IPs calculated for relaxed and unrelaxed surfaces were shown to be small in Ref. 25.

4 Results and discussion

4.1 Electronic matching of junction partners

Table 1 Calculated ionisation potentials (IP), electron affinities (χ), HSE06 band gaps (E_g) all in units of eV and unrelaxed surface energies (γ) in units of eV per \AA^2 for symmetric and non-polar slab models of enargite (Cu_3AsS_4) and bournonite (CuPbSbS_3).

Absorber	Termination	E_g	IP	χ	γ
Enargite (Cu_3AsS_4)	(100)	1.32	4.97	3.64	0.050
	(010) a	1.32	5.21	3.89	0.025
	(010) b	1.32	6.23	4.91	0.120
	(110)	1.32	4.95	3.63	0.070
Bournonite (CuPbSbS_3)	(100)	1.68	5.61	3.93	0.042
	(010) a	1.68	5.20	3.52	0.150
	(010) b	1.68	5.21	3.53	0.106
	(110) a	1.68	6.50	4.82	0.090
	(110) b	1.68	6.04	4.36	0.037

Band energies are calculated for all symmetric, non-polar surfaces as outlined in the methodology section and are presented in Table 1 where, for example, (110)a and (110)b simply refers to an alternative termination for the same crystal plane direction. We find that there is a notable variation in the IP of different surface terminations of the same material, which may have implications for the simplicity of the junction fabrication, especially as the minimum energy surface

terminations have significantly different IPs. From inspection of the slab geometries (shown in the SI), generally slab models with larger IPs have denser surfaces and are more anion-terminated. This observation could be attributed to greater electron ‘spillage’ into the vacuum from dense, anion-terminated surfaces resulting in a greater surface double layer and surface dipole³⁵, thereby requiring more energy to remove an electron from the surface.

Experimental data available for enargite suggests that the material exhibits p-type intrinsic conductivity^{36,37}. For bournonite, there is contradiction in the literature between experimental measurements on natural samples measuring n-type conductivity³⁷ and theoretical prediction of the defect physics suggesting the material will be intrinsically p-type and difficult to dope n-type³⁸. Junction partners for enargite are screened for based on the CBO only, while for bournonite the CBO and VBO are each considered in turn to provide options for the material as either a p-type or n-type absorber layer. We screen for small cliff offsets for bournonite and enargite but also screen for spike offsets if calculated effective masses for minority carriers are less than our threshold of $0.5m_e$. For bournonite therefore we screen for both cliff and spike CBO for p-type bournonite, but only for a cliff VBO for n-type bournonite due to calculated heavy holes⁸. For enargite we screen for candidate junction partners for a cliff and a spike CBO.

4.2 Minimum strain junction partners

Candidates from the electronic band offset screening step were then screened further to find candidates for which it was possible to construct an interface with the absorber that produced less than 4% strain. Candidates containing Fe were not considered further as Fe is associated with ‘killer defects’ in many cases due to many possible excitations and recombination channels from a half occupied d -shell (d^5 for Fe^{3+} and d^6 for Fe^{2+}). Where multiple structure files for the candidates were available on the Materials Project database³⁹, conventional unit cells for the most stable structures were preferentially selected for this lattice matching step, based on energy above the convex hull. Candidates in the Materials Project database with approximate band gaps closer to the desirable range for junction partners were also preferentially selected, taking into account the stated underestimation of the band gap from the Materials Project high-throughput calculations of approximately 40%^{40,41}. Although it is also worth noting that the band alignment may vary for different polymorphs of the junction partner, as has been demonstrated for the $\text{Cu}_2\text{ZnSnS}_4\text{:CdS}$ interface²⁸. A table containing all candidates considered in this second screening step, including the materials project ID for the corresponding structure file, can be found in the SI.

Each slab model termination was screened individually, in

each case starting from the tabulated data for 173 candidate heterojunction partners and the remaining candidates for each surface model are shown in Tables 2 and 3 for bournonite and enargite respectively. Averaged in-plane interface strains for all minimum strain electronically matched candidate junction partners are also contained in Tables 2 and 3. Examples of band alignment plots are shown in Fig. 3 and 4 but plots for all other slab terminations are included in the SI. In each case, the minimum strain candidate junction partner is shown in the bolder colour.

4.2.1 Junction partners for bournonite As shown in Table 1, the lowest energy surfaces for bournonite were for the (100) and (110)b terminations. We will therefore discuss the most promising candidate junction partners for these terminations in the most detail. For the bournonite (100) surface, we were only able to find junction partners able to produce an interface strain below the threshold for a CBO cliff, which is relevant for bournonite as a p-type absorber. Table 2 shows several options for junction partners for this type of offset, however, more intermixing may be expected between a S containing absorber and ZnSe, as has been shown to be the case for the CdS:CuIn(S,Se)₂ interface with S/ Se intermixing⁴³. Substantial intermixing could firstly make our calculated band offsets less applicable, but also could produce parasitic secondary phases. Another consideration is the simplicity of junction fabrication. Candidate junction partners able to produce an interface with interfacial strain below the threshold for multiple facets of the junction partner may imply more robust synthesis. For these reasons, although Fig. 3a shows SnS₂ to be the minimum strain candidate, we propose GaP and Ce₂O₃ as the better options as both had three terminations with low-strain interfaces with this termination of bournonite.

For the bournonite (110)b termination we were able to find candidate junction partners for a spike CBO, cliff CBO and cliff VBO. We therefore present options for bournonite as both a p-type and n-type absorber. It is possible that there could be significant intermixing between a S containing absorber and a Te containing junction partner, as has been observed at the CdTe: CdS interface²³, for this reason the oxide or sulfide candidate junction partners may be more desirable, despite ZnTe being shown as the minimum strain candidate in Fig. 3d. Again in the interests of robust junction synthesis, candidates where various facets produce a low strain interface may also be more desirable. Table 2 shows various options for junction partners that meet these criteria and the associated interface strain.

4.2.2 Junction partners for enargite Table 1 shows that for enargite the (010)a termination is the lowest energy with the next being the (100) and (110) terminations with similar energies. We firstly note that although CdS is in our database of candidate junction partners, it did not make it through

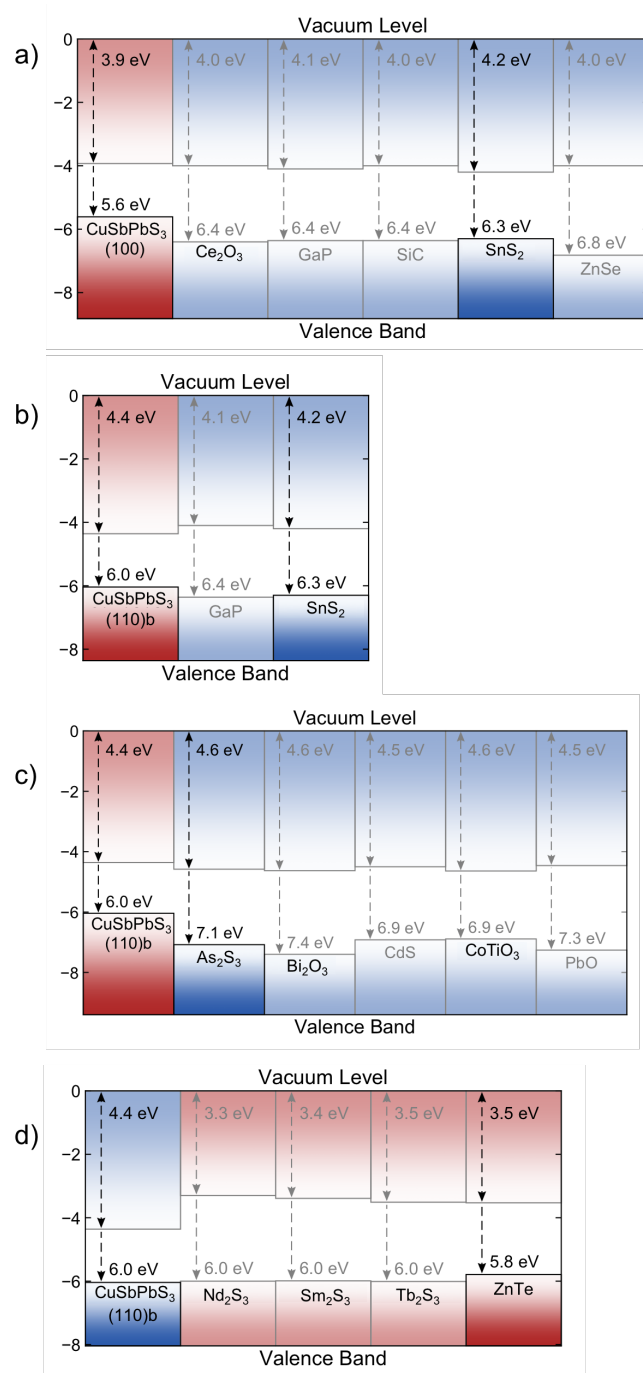


Fig. 3 Candidate junction partners for p-type bournonite (CuPbSbS₃) absorber layer termination (100) for a) a cliff conduction band offset (CBO), b) (110)b termination for a spike CBO, c) cliff CBO and d) cliff VBO for n-type bournonite absorber. Minimum strain junction partner is shown in bold. Band alignment plots produced using the bapt software package⁴².

Table 2 Minimum strain terminations and in-plane averaged interface strain of candidate solar cell heterojunction partners after electronic band and lattice matching for the absorber bournonite (CuPbSbS₃) allowing for the absorber to be either p-type (through electronic matching of conduction bands via the CBO) or for an n-type absorber (through matching of the valence bands via the VBO).

Bournonite(100) CBO cliff								
			Candidate	Min. strain term.(s)	Av. strain			
			Ce ₂ O ₃	(011), (101), (110)	1.23%			
			GaP	(011), (101), (110)	1.01%			
			SiC	(010), (100)	0.73%			
			SnS ₂	(110)	0.67%			
			ZnSe	(001), (010), (100)	0.83%			
Bournonite(010)a CBO spike			Bournonite(010)a CBO cliff			Bournonite(010)a VBO cliff		
Candidate	Min. strain term.(s)	Av. strain	Candidate	Min. strain term.(s)	Av. strain	Candidate	Min. strain term.(s)	Av. strain
La ₂ S ₃	(110)	0.71%	Ce ₂ S ₃	(001)	1.71%	AlP	(011), (101), (110)	0.71%
Nd ₂ S ₃	(001)	0.10%	Cu ₂ O	(011), (101), (110)	0.81%	MoO ₃	(100)	0.23%
Sm ₂ S ₃	(001)	2.28%	Gd ₂ S ₃	(011)	0.71%	CuI	(110)	2.73%
WO ₃	(110)	0.49%	ZnTe	(001), (010), (100)	0.75%			
Bournonite(010)b CBO spike			Bournonite(010)b CBO cliff			Bournonite(010)b VBO cliff		
Candidate	Min. strain term.(s)	Av. strain	Candidate	Min. strain term.(s)	Av. strain	Candidate	Min. strain term.(s)	Av. strain
La ₂ S ₃	(110)	0.71%	Ce ₂ S ₃	(001)	1.71%	AlP	(011), (101), (110)	0.71%
Nd ₂ S ₃	(001)	0.10%	Cu ₂ O	(011), (101), (110)	0.81%	MoO ₃	(100)	0.23%
Sm ₂ S ₃	(001)	2.28%	Gd ₂ S ₃	(011)	0.71%	CuI	(110)	2.73%
WO ₃	(110)	0.49%	ZnTe	(001), (010), (100)	0.75%			
Bournonite(110)a CBO spike						Bournonite(110)a VBO cliff		
Candidate	Min. strain term.(s)	Av. strain				Candidate	Min. strain term.(s)	Av. strain
As ₂ S ₃	(101)	0.90%				Ce ₂ O ₃	(011), (101), (110)	0.68%
Bi ₂ O ₃	(100)	1.60%				GaP	(011), (101), (110)	1.35%
CoTiO ₃	(110)	1.03%				SnS ₂	(010), (100)	0.94%
NiTiO ₃	(110)	1.08%				WO ₃	(010)	1.00%
						Zn ₃ In ₂ S ₆	(110)	0.09%
						Dy ₂ S ₃	(110)	1.47%
						SiC	(110)	1.47%
Bournonite(110)b CBO spike			Bournonite(110)b CBO cliff			Bournonite(110)b VBO cliff		
Candidate	Min. strain term.(s)	Av. strain	Candidate	Min. strain term.(s)	Av. strain	Candidate	Min. strain term.(s)	Av. strain
GaP	(011), (101), (110)	1.35%	As ₂ S ₃	(101)	0.90%	Nd ₂ S ₃	(110)	0.64%
SnS ₂	(101), (100)	0.94%	Bi ₂ O ₃	(100)	1.60%	Sm ₂ S ₃	(110)	0.70%
			CdS	(110)	2.17%	Tb ₂ S ₃	(110)	1.71%
			CoTiO ₃	(110)	1.03%	ZnTe	(011), (101), (110)	0.43%
			PbO	(110)	1.67%			

Table 3 Identified low-strain terminations and in-plane averaged interface strain of candidate solar cell heterojunction partners for p-type enargite (Cu_3AsS_4) after electronic band and lattice matching.

Enargite(100) spike CBO					
Candidate	Min. strain term.(s)	Av. strain			
Dy ₂ S ₃	(001)	0.81%			
Sm ₂ S ₃	(001)	1.43%			
Tb ₂ S ₃	(001)	1.10%			
ZnTe	(011), (101), (110)	1.01%			
Enargite(010)a spike CBO			Enargite(010)a cliff CBO		
Candidate	Min. strain term.(s)	Av. strain	Candidate	Min. strain term.(s)	Av. strain
Ce ₂ S ₃	(001)	1.05%	Ce ₂ O ₃	(001), (010), (100)	0.20%
Zn ₃ In ₂ S ₆	(110)	1.19%	GaP	(001), (010), (100)	0.83%
			SiC	(010), (100)	1.33%
			ZnSe	(001), (010), (100)	2.02%
Enargite(010)b spike CBO					
Candidate	Min. strain term.(s)	Av. strain			
Bi ₂ O ₃	(101)	0.75%			
Enargite(110) spike CBO					
Candidate	Min. strain term.(s)	Av. strain			
Dy ₂ S ₃	(011), (101)	0.68%			
Sm ₂ S ₃	(001)	1.15%			
Tb ₂ S ₃	(011), (101)	0.98%			
WO ₃	(011)	0.33%			
ZnTe	(011), (101), (110)	0.19%			

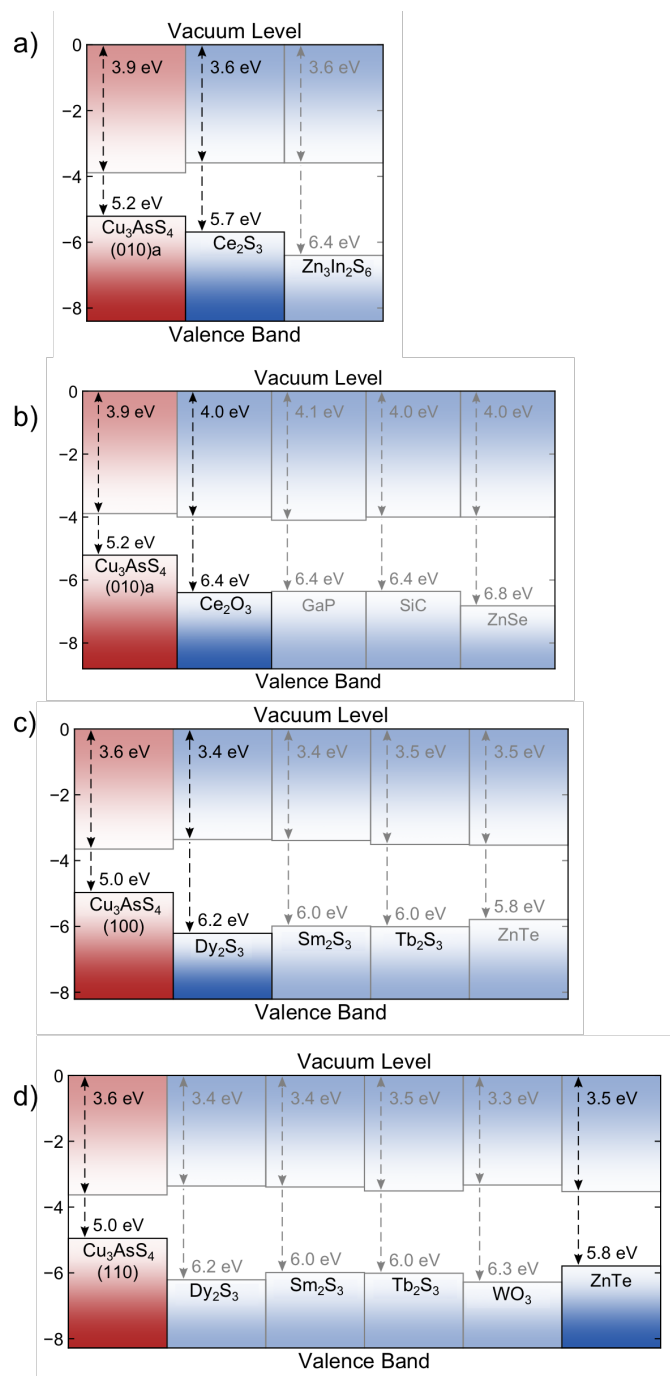


Fig. 4 Candidate junction partners for p-type enargite (Cu_3AsS_4) absorber layer termination (010)a for a) spike conduction band offset (CBO), b) cliff CBO, c) spike CBO for (100) termination and d) spike CBO for (110) termination. Minimum strain junction partner is shown in bold. Band alignment plots produced using the bapt software package⁴².

the screening process for any surface termination of enargite. Therefore, this could be one possible explanation for the low open circuit voltage of enargite solar cells fabricated with CdS as the junction partner in Ref. 9.

For the minimum energy (010)a termination of enargite, junction partners with an interface strain below the threshold were found for both a cliff and a spike CBO. This data is shown in Table 3. In the case of the spike offset only one termination of each junction partner candidate produced a low strain interface, possibly implying more complex growth procedures would be required. For the cliff CBO for the (010)a enargite termination, most candidate junction partners had several terminations able to produce a low-strain interface. However, again a Se containing junction partner may also result in more intermixing at an interface with a S containing absorber. For this termination, Ce_2O_3 appears to be the most promising candidate junction partner for having multiple terminations able to produce the least interface strain.

For the (100) and (110) terminations of enargite, only minimum-strain candidates were found for a spike CBO but both terminations had a similar list of candidate junction partners. Dy_2S_3 produced the lowest strain interface with the enargite (100) surface and ZnTe with the (110) surface, but both candidates produced low-strain interfaces with the enargite (100) and (110) surfaces. ZnTe may be a good option for more robust synthesis as more terminations of the latter junction partner resulted in interfaces below the strain threshold. However, again, it may be expected that there would be more intermixing at an interface with a telluride junction partner than with a sulfide or oxide.

4.2.3 Non-ideal interfaces We have considered the likely extent of intermixing of the absorber layers with the most promising junction partner candidates, however we have not yet discussed the likely impact of finite temperature on the electronic band offsets or of Fermi level pinning from interface defects. Firstly for the latter, we aimed to reduce the likely concentration of interface defects from our minimal interface strain screening step. However, we still cannot rule out the impact of interface defects. To fully understand the impact of finite temperatures on the electronic band offsets, further investigations into thermal lattice expansion and electron-phonon coupling in the materials would be necessary, as has been done for the $\text{Cu}_2\text{ZnSnS}_4\text{:CdS}$ interface in Ref. 28. That study showed that thermal effects could alter the band offset by 0.07 eV, whilst this is important for optimisation of the device, the accuracy of the methods applied in our study are more appropriate for rapid screening and identification of promising lead materials for junction partners.

5 Conclusions

The purpose of this work is to provide a starting point for further investigations into optimal device architectures to accelerate the development of these new solar cell technologies. We have screened a database of 173 semiconductor materials and identified ~5 promising photovoltaic heterojunction partners for each surface termination of enargite (Cu_3AsS_4) and bournonite (CuPbSbS_3). We have discussed the limitations of our predictions and highlighted the areas for further study. By using a combination of data mining and first principles calculation we have accelerated the design of optimal architectures for these promising new photoferroic materials. The intention is to enable the exploration of possible effects of ferroelectricity or at least internal electric fields of polar crystals in photovoltaic devices. One such possibility is suppressed electron-hole recombination by enhanced local carrier separation due to the internal electric fields⁷ to provide a new means of achieving high-efficiency solar cells. Another possible route to explore in such devices is the potential for tunability of charge transport across interfaces by the direction of electric polarisation as has been explored in photoanodes for photoelectrochemical water splitting applications⁴⁴.

6 Data access

Link to MacroDensity and ELS repos (inc. my fork for interactive script or just add link in main repo as example? - Check with Keith) + relaxed unit cell POSCARs used to cut slabs and slabs cut by Yoyo?

7 Acknowledgements

We thank Jake Bowers, Elisabetta Arca, Ji-Sang Park and Lee Burton for discussions. This work has been supported by the EPSRC grant no. EP/L016354/1 and EP/K016288/1 (SKW). This work benefited from access to ARCHER, the UK's national high-performance computing service, which is funded by the Office of Science and Technology through EPSRC's High End Computing Programme (Grant no. EP/L000202).

References

- 1 V. M. Fridkin and B. N. Popov, *Soviet Physics Uspekhi*, 1978, **21**, 981.
- 2 W. Ruppel, R. V. Baltz and P. Wurfel, *Ferroelectrics*, 1982, **43**, 109–123.
- 3 K. T. Butler, J. M. Frost and A. Walsh, *Energy and Environmental Science*, 2015, **8**, 838–848.
- 4 S. M. Young and A. M. Rappe, *Physical Review Letters*, 2012, **109**, 116601.
- 5 H. Heyszenau, *Physical Review B*, 1978, **18**, 1586–1592.
- 6 F. Wang and A. M. Rappe, *Physical Review B*, 2015, **91**, 165124.

- 7 P. Lopez-Varo, L. Bertoluzzi, J. Bisquert, M. Alexe, M. Coll, J. Huang, J. A. Jimenez-Tejada, T. Kirchartz, R. Nechache, F. Rosei and Y. Yuan, *Physics Reports*, 2016, **653**, 1–40.
- 8 S. K. Wallace, K. L. Svane, W. P. Huhn, T. Zhu, D. B. Mitzi, V. Blum and A. Walsh, *Sustainable Energy Fuels*, 2017, **1**, 1339–1350.
- 9 S. A. McClary, J. Andler, C. A. Handwerker and R. Agrawal, *J. Mater. Chem. C*, 2017, **5**, 6913–6916.
- 10 T. J. Whittles, T. D. Veal, C. N. Savory, A. W. Welch, F. W. de Souza Lucas, J. T. Gibbon, M. Birkett, R. J. Potter, D. O. Scanlon, A. Zakutayev and V. R. Dhanak, *ACS Applied Materials & Interfaces*, 2017.
- 11 F. Larsson, N. S. Nilsson, J. Keller, C. Frisk, V. Kosyak, M. Edoff and T. Törndahl, *Progress in Photovoltaics: Research and Applications*, 2017.
- 12 A. Crovetto and O. Hansen, *Solar Energy Materials and Solar Cells*, 2017, **169**, 177–194.
- 13 A. Klein, *Journal of Physics: Condensed Matter*, 2015, **27**, 134201.
- 14 K. T. Butler, Y. Kumagai, F. Oba and A. Walsh, *J. Mater. Chem. C*, 2016, **4**, 1149–1158.
- 15 J. Nelson, in *The Physics of Solar Cells*, Imperial College Press, 2003, ch. 8.
- 16 T. Song, A. Kanevce and J. R. Sites, *Journal of Applied Physics*, 2016, **119**, 233104.
- 17 E. Arca, A. Fioretti, S. Lany, A. C. Tamboli, G. Teeter, C. Melamed, J. Pan, K. N. Wood, E. Toberer and A. Zakutayev, *IEEE Journal of Photovoltaics*, 2018, **8**, 110–117.
- 18 A. J. Heeger, *Advanced Materials*, 2013, **26**, 10–28.
- 19 R. Hoffman and J. Wager, *Thin Solid Films*, 2003, **436**, 286–291.
- 20 S. Oktyabrsky, *L21-heterojunctions*, 2004 (Accessed on June 21, 2018).
- 21 M. Gloeckler and J. Sites, *Thin Solid Films*, 2005, **480–481**, 241–245.
- 22 D. T. F. Marple, *Physical Review*, 1963, **129**, 2466–2470.
- 23 K. Ohata, J. Saraie and T. Tanaka, *Japanese Journal of Applied Physics*, 1973, **12**, 1641.
- 24 J.-S. Park, J.-H. Yang, T. Barnes and S.-H. Wei, *Applied Physics Letters*, 2016, **109**, 042105.
- 25 Y. Kumagai, K. T. Butler, A. Walsh and F. Oba, *Physical Review B*, 2017, **95**, year.
- 26 R. L. Anderson, *IBM Journal of Research and Development*, 1960, **4**, 283–287.
- 27 K. T. Butler, Y. Kumagai, F. Oba and A. Walsh, *J. Mater. Chem. C*, 2016, **4**, 1149–1158.
- 28 B. Monserrat, J.-S. Park, S. Kim and A. Walsh, *Applied Physics Letters*, 2018, **112**, 193903.
- 29 Y. Hinuma, Y. Kumagai, F. Oba and I. Tanaka, *Computational Materials Science*, 2016, **113**, 221–230.
- 30 G. Kresse and J. Furthmüller, *Computational Materials Science*, 1996, **6**, 15–50.
- 31 G. Kresse and J. Furthmüller, *Physical Review B*, 1996, **54**, 11169–11186.
- 32 G. I. Csonka, J. P. Perdew, A. Ruzsinszky, P. H. T. Philipsen, S. Lebègue, J. Paier, O. A. Vydrov and J. G. Ángyán, *Physical Review B*, 2009, **79**, 155107.
- 33 P. E. Blöchl, *Physical Review B*, 1994, **50**, 17953–17979.
- 34 J. Heyd, G. E. Scuseria and M. Ernzerhof, *The Journal of Chemical Physics*, 2003, **118**, 8207–8215.
- 35 J. Bardeen, *Physical Review*, 1936, **49**, 653–663.
- 36 T. Pauporte and D. Lincot, *Advanced Materials for Optics and Electronics*, 1995, **5**, 289–298.
- 37 B. Durant and B. A. Parkinson, 2016 IEEE 43rd Photovoltaic Specialists Conference (PVSC), 2016.
- 38 A. Faghaninia, G. Yu, U. Aydemir, M. Wood, W. Chen, G.-M. Rignanes, G. J. Snyder, G. Hautier and A. Jain, *Physical Chemistry Chemical Physics*, 2017, **19**, 6743–6756.
- 39 A. Jain, S. P. Ong, G. Hautier, W. Chen, W. D. Richards, S. Dacek, S. Cholia, D. Gunter, D. Skinner, G. Ceder and K. a. Persson, *APL Materials*,

-
- 2013, **1**, 011002.
- 40 A. Jain, S. P. Ong, G. Hautier and C. Moore, *Calculations guide*, <https://materialsproject.org/docs/calculations>, Accessed: 2018-09-03.
- 41 A. Jain, G. Hautier, C. J. Moore, S. P. Ong, C. C. Fischer, T. Mueller, K. A. Persson and G. Ceder, *Computational Materials Science*, 2011, **50**, 2295 – 2310.
- 42 A. Ganose, *Band alignment plotting tool*, <https://github.com/utf/bapt>, Accessed: 2018-09-24.
- 43 L. Weinhardt, M. Bär, S. Pookpanratana, M. Morkel, T. P. Niesen, F. Karg, K. Ramanathan, M. A. Contreras, R. Noufi, E. Umbach and C. Heske, *Applied Physics Letters*, 2010, **96**, 182102.
- 44 W. Yang, Y. Yu, M. B. Starr, X. Yin, Z. Li, A. Kvit, S. Wang, P. Zhao and X. Wang, *Nano Letters*, 2015, **15**, 7574–7580.